

## A numerical study on the influence of geometry on the rupture risk of abdominal aortic aneurysms

G R Krishna Chand Avatar,<sup>1, a)</sup> Chinika Dangi,<sup>b)</sup> and Puneet Pushkar<sup>c)</sup>

*Department of Aerospace Engineering, Indian Institute of Science, Bangalore, India*

(Dated: 27 November 2023)

Abdominal aortic aneurysms (AAAs) are local dilatations in the abdominal aorta occurring due to weakening of arterial wall due to various factors such as intraluminal thrombus, old age, male gender and hypertension. Hemodynamic parameters, such as, wall shear stress (WSS), and maximum aneurysmal wall stress are typically used to assess rupture risk of AAAs. Generally, patient-specific AAAs can be characterised by geometric shape indices derived from maximum transverse diameter, neck diameters and abdominal height. The influence of one such shape index DHr, the ratio of maximum transverse diameter to abdominal height, on AAA biomechanics is investigated for two AAA geometries, AAA1 of higher DHr than AAA2, with the help of hemodynamics and AAA wall mechanics simulations. Blood is modeled as Newtonian and non-Newtonian Carreau-Yasuda fluids. Newtonian case overpredicts WSS and time-averaged WSS (*TAWSS*) and has lower oscillatory shear index (*OSI*). AAA1 has lower *TAWSS*, higher *OSI* and higher WSS spatial gradient than AAA2 suggesting that the former has increased susceptibility to thrombus deposition and, therefore, higher risk of AAA rupture. Three constitutive models are used to describe the behaviour of AAA wall, namely, linear elastic, Saint Venant Kirchhoff elastic and a phenomenological finite-strain model for AAAs proposed by Raghavan et al. (J. Biomech. (2000) 33:475-482) called Raghavan-Vorp elastic. Raghavan-Vorp model produces the highest peak wall stress than the other two models. The peak wall stress of AAA1 is about 8 % higher than that of AAA2 indicating that the former is at a greater risk of rupture. It is concluded that higher DHr leads to increased risk of rupture of AAAs.

---

<sup>a)</sup>krishnaagr@iisc.ac.in

<sup>b)</sup>chinikadangi@iisc.ac.in

<sup>c)</sup>puneetp@alum.iisc.ac.in

## I. INTRODUCTION

An arterial aneurysm is a vascular condition characterized by an abnormal focal dilatation of an artery with respect to its original state<sup>1-3</sup>. This happens due to localised bulging of blood vessels as a result of the weakening of the arterial walls<sup>4</sup>. Aneurysm shapes could be saccular (asymmetric balloon-like expansions of a portion of the wall), fusiform (axisymmetric gradual dilatation of the entire circumference of the artery) or cylindroid<sup>5</sup>. Aortic aneurysms are located either in the thoracic region or in the infrarenal segment, that is, the abdominal region between the renal arteries and the iliac bifurcation; the latter is called abdominal aortic aneurysm (Fig. 1) and is nearly 80 % of all aortic aneurysms. An abdominal aortic aneurysm (AAA) is also defined as an infrarenal segment with aortic diameter at least 1.5 times the normal diameter of the renal arteries, which is approximately 2 cm<sup>2,3</sup>.

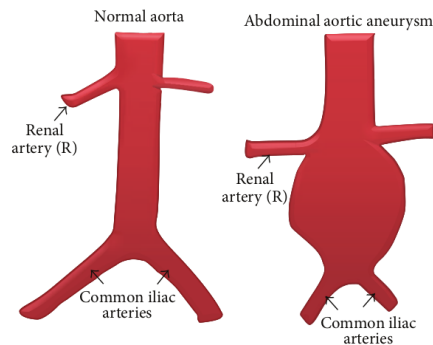


FIG. 1: Schematic of normal aorta and abdominal aortic aneurysm. Source:<sup>1</sup>

While there is no official statistics on patients with AAAs in India published by the relevant health authorities, Unnikrishnan et al.<sup>6</sup> have deduced, based on their study, that the incidence of AAAs in India is very low compared to the Western countries. There are several risk factors responsible for the genesis, growth and rupture of AAAs, namely, people aged above 60 years, smoking, males, patients with atherosclerosis, coronary heart disease and hypertension<sup>7-9</sup>. Other predisposing factors to AAA include a positive family history; risk of AAA increases 4 times for a patient whose first-degree relative underwent surgical repair for AAA<sup>2</sup>. Rupture risk of an AAA is influenced by multiple factors including aneurysm size, expansion rate and sex.

AAAs are severe medical conditions often requiring surgical management. They are detected incidentally when performing ultrasonography, abdominal computed tomography

or magnetic resonance imaging for unrelated causes<sup>2</sup>. AAAs are often asymptomatic until they suddenly rupture, which necessitates a measure of rupture risk prediction. Typically, surgeons tend to use a criterion based on maximum transverse diameter to decide on the course of treatment. Fusiform AAAs with diameter larger than 5-5.5 cm and an expansion rate of 1 cm/year are recommended for surgical repair while those smaller than 4 cm are considered to be at low risk of rupture<sup>10</sup>. However, this criterion has been deemed crude by various researchers<sup>5,10-14</sup> since there have been instances when aneurysms of diameter smaller than 4 cm ruptured while those with diameter greater than the critical transverse diameter did not<sup>15</sup>; thus necessitating detailed hemodynamics and wall mechanics studies to identify the parameters directly and indirectly responsible for the rupture of AAAs. These parameters include wall shear stress and its derivatives, and aneurysmal wall stress.

### A. Role of numerical simulations for the study of aneurysms

Bluestein et al.<sup>16</sup> concluded, based on steady state computational fluid dynamics (CFD) simulation of an axisymmetric aneurysm, that fluid dynamics characterising flow recirculation region formed inside the aneurysm created suitable conditions encouraging thrombus formation and the viability of aneurysm rupture. Boyd et al.<sup>14</sup> conducted a CFD study on 7 ruptured AAAs with maximum diameter  $8.3 \pm 0.9$  cm and observed that aortic rupture took place at the sites of reduced flow velocity, mostly, in recirculation flow regions, where low WSS and relatively more intraluminal thrombus deposition persisted but not at the site of maximum pressure and wall shear stress (WSS). Finol et al.<sup>13</sup> did CFD simulations of patient-specific aneurysm models to quantify vortex dynamics and flow-induced WSS distributions in the aneurysms in the absence of ILT and learnt that the vortex dynamics is specific to every individual and is dependent on the shape and size of the aneurysm. Lin et al.<sup>17</sup> investigated the influence of modeling techniques — fluid-solid interaction (FSI), CFD and Computational solid stress (CSS) approaches – and material models for AAA wall – isotropic and anisotropic – when conducting numerical simulations on a clinical AAA model, saccular in shape. They observed that CFD approach led to the formation of smaller vortices and overestimated wall shear stress as compared to FSI. Philip et al.<sup>4</sup> postulated that high time-averaged wall shear stress (TAWSS) and low oscillatory shear index (OSI) indicates the initiation of intraluminal thrombus (ILT) formation. However as AAA expands, the

ILT growth reduces the lumen of the AAA and decreasing TAWSS and eventually during the phase of rupture, low TAWSS is observed at the regions where heavy thrombus growth takes place<sup>14</sup>.

Vorp et al.<sup>11</sup> concluded that aneurysm rupture occurs when the mechanical stress acting on the aneurysm inner wall due to intraluminal pressure, exceeds the failure strength of the degenerated aortic tissue.

Raghavan et al.<sup>18</sup> conducted an experimental study on tissue samples gathered from 78 people (71 had AAAs and the rest had normal abdominal aorta), and provided a comparison of failure strengths of aneurysmal versus nonaneurysmal tissue. It was observed that yield strength reduced by nearly 50 % and ultimate strength reduced by over 50 % for AAAs with respect to the normal aorta. Venkatasubramaniam et al.<sup>15</sup> found that peak wall stress was significantly higher in the ruptured AAA and also discovered that the area of peak wall stress correlated with rupture site.

Scotti et al.<sup>19</sup> studied how variation of wall thickness and geometry asymmetry affects the wall stress in a model AAA and observed that an asymmetric AAA with regional variations in wall thickness saw much higher mechanical stresses, about 4 times, than a fusiform AAA with uniform wall thickness, and therefore at more risk of rupture. However since it is quite difficult to measure wall thickness noninvasively, a uniform thickness of 1.2-1.5 mm is typically assumed for biomechanical modelling of AAAs<sup>20</sup>.

Perez et al.<sup>21</sup> performed a steady state FEM analysis on 190 AAA geometries generated using 18 input parameters (obtained from Martufi et al.<sup>20</sup>) and concluded that the maximum principal wall stress could be predicted to a reasonable accuracy by measuring maximum diameter, wall thickness, the Euclidean distance between centroids at the maximum and inlet cross-sections, and the tortuosity of AAA; all these parameters can be obtained with modern and inexpensive clinical imaging technology.

## B. Problem description

Martufi et al.<sup>20</sup> extracted 3D patient-specific geometries from Computed Tomography (CT) images of nine patients with AAA. An idealized 3D axisymmetric fusiform-shaped aneurysm with volume equal to the average volume of the nine AAAs was used to evaluate 9 1D geometric indices (see Fig. 2), namely, maximum transverse diameter  $D_{max}$ , proximal

neck diameter  $D_{neck1}$  immediately below the renal arteries (if no neck is present, it is calculated as the smallest diameter distal to the renal arteries), distal neck diameter  $D_{neck2}$ , abdominal height  $H$ , length of centerline from neck to distal end of AAA  $L$ , the bulge height  $H_b$  (if no neck is present, it is calculated as the smallest diameter distal to the renal arteries), the distance between the lumen centroid and the centroid of the cross section where  $D_{max}$  is located  $d_c$ , the Euclidean distance from the centroid of the cross-section where  $D_{neck1}$  is located to the centroid of the cross section at the AAA distal end  $d$  and the length of the curve joining the centroids of proximal and distal neck cross-sections  $L_{neck}$ .

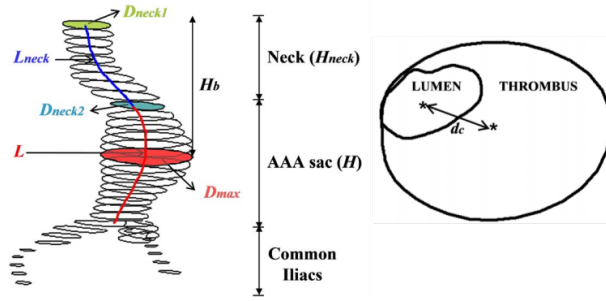


FIG. 2: Geometric indices defined by Martufi et al.<sup>20</sup> based on patient-specific AAA geometries extracted from CT images

Using these geometric indices, six 2D shape indices were derived, namely diameter-height ratio (DHr), diameter-diameter ratio (DDr), height ratio (Hr), bulge location (BL), asymmetry factor ( $\beta$ ), and tortuosity (T) which were defined as

$$\text{DHr} = \frac{D_{max}}{H}, \text{DDr} = \frac{D_{max}}{D_{neck1}}, \text{Hr} = \frac{H}{H_{neck}}, \text{BL} = \frac{H_b}{H}, \beta = 1 - \frac{d_c}{D_{max}}, T = \frac{L}{d}$$

Due to severe constraints in generating computer-aided design (CAD) geometries for non-trivial shape indices, we have to reduce our indicial parametric space to obtain less complex geometries for carrying out numerical studies of AAAs. In order to obtain idealised geometries, we consider  $\beta = T = 1$  to get fusiform AAAs, thus reducing the dimension of parametric space to 4; the remaining 4 indices are DHr, DDr, Hr and BL. Martufi et al.<sup>20</sup> have suggested that the patient-specific DDr index would be a more accurate parameter for personalized assessment of aneurysm size and also its eventual rupture, instead of the common criterion of AAA maximum diameter. This was confirmed by some researchers (Cappeler et al.<sup>22</sup>). However, Philip et al.<sup>4</sup> did fluid-structure interaction (FSI) simulations

on 5 AAA geometries and suggested that the shape index DHr could be the most important factor in assessing the aneurysm risk prediction and requires further detailed analysis.

The present work attempts to investigate the influence of DHr on both hemodynamics and arterial wall mechanics using more realistic constitutive models. We have modeled blood using both Newtonian and non-Newtonian (Carreau-Yasuda) constitutive relations. The AAA wall has been modeled using both linear elastic and non-linear elastic (Saint Venant Kirchhoff elastic and Raghavan-Vorp elastic<sup>23</sup>) models. We consider two AAA geometries, AAA1 and AAA2, for our study (the one with highest DHr studied by Philip et al.<sup>4</sup> and the equivalent fusiform AAA geometry in Martufi et al.<sup>20</sup>) whose shape indices are

	AAA1	AAA2
DHr	0.83	0.45
DDr	2	2
Hr	2.4	3.67
BL	0.92	0.77

## II. METHODOLOGY

Physically, the aneurysm problem is composed of two sub-parts, namely, fluid part and solid part. The fluid part involves computation of the flow dynamics of blood through the AAA lumen (fluid domain) while the solid part involves computing displacement of the elastic arterial and aneurysm wall (solid domain) due to traction exerted on its endoluminal surface by the blood flow. Mathematically, the geometry of the aneurysm problem is denoted by a domain  $\Omega$ , with boundary  $\Gamma$ , which is composed of a solid domain  $\Omega^s$  and a fluid domain  $\Omega^f$ , such that  $\Omega = \Omega^s \cup \Omega^f$ , alongwith their corresponding boundaries  $\Gamma^s$  and  $\Gamma^f$ <sup>24</sup> as shown in Fig. 3. The fluid-solid interface is  $\Gamma^{fs} = \Gamma^f \cap \Gamma^s$ ; this acts as the wall for fluid domain).

### A. Fluid dynamical model for Blood

We consider blood to be an incompressible fluid, in an isothermal flow regime. Blood shows both shear-thinning and viscoelastic behaviour due to red blood cells (RBCs) which

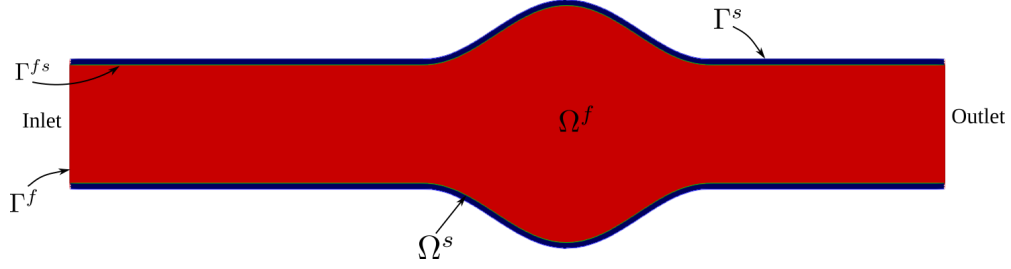


FIG. 3: Fluid domain  $\Omega^f$  with boundary  $\Gamma^f$  enclosing it, solid domain  $\Omega^s$  with its corresponding boundary  $\Gamma^s$ , and fluid-solid interface  $\Gamma^{fs}$

constitute about 99 % of all the cells in the blood. Sequeira et al.<sup>25</sup> have stated that blood flow displays predominantly Newtonian behaviour as it circulates through large arteries. However, Khanafer et al.<sup>26</sup> have concluded that the blood flow may be affected by non-Newtonian behaviour of blood in pathological vascular conditions such as AAAs where RBCs and platelets can aggregate resulting in the change of viscosity. Additionally, Cho et al.<sup>27</sup> observed that the non-Newtonian model of blood yields higher wall shear stress than the Newtonian one in flow separation or recirculation regions. Therefore, we carry out numerical simulations using both Newtonian and non-Newtonian Carreau-Yasuda models for the blood with material parameters taken from Biasseti et al<sup>28</sup>. The blood density is  $\rho = 1050 \text{ kg/m}^3$  and the transport properties for the two models are taken from<sup>28</sup>

- Newtonian model: dynamic viscosity  $\mu^f = 0.0044 \text{ Pa-s}$
- Carreau-Yasuda model: dynamic viscosity  $\mu^f = \mu_\infty + (\mu_0 - \mu_\infty)[1 + (\lambda\dot{\gamma})^a]^{(n-1)/a}$  where  $\mu_0 = 0.16 \text{ Pa-s}$ ,  $\mu_\infty = 0.0035 \text{ Pa-s}$ ,  $\lambda = 8.2 \text{ s}$ ,  $n = 0.2128$ ,  $a = 0.64$

### 1. *Mathematical model*

The governing equations are derived from the conservation of mass and balance of linear momentum are expressed in integral form as

- Mass conservation equation:  $\int_S \rho^f \mathbf{v}^f \cdot \mathbf{n} dS = 0$
- Momentum balance equation, neglecting body forces:  $\frac{\partial}{\partial t} \int_V \rho^f \mathbf{v}^f(\mathbf{x}, t) dV + \oint_{S(t)} \rho^f \mathbf{v}^f \mathbf{v}^f \cdot \mathbf{n} dS = \oint_{S(t)} \boldsymbol{\sigma}^f \cdot \mathbf{n} dS$

The constitutive relation relating the Cauchy stress tensor to the velocity field for a Newtonian fluid is given as  $\boldsymbol{\sigma}^f = -p\mathbf{I} + \mu^f \left( \nabla \mathbf{v}^f + (\nabla \mathbf{v}^f)^T \right) - \frac{2}{3} \mu^f (\nabla \cdot \mathbf{v}^f) \mathbf{I}$  where  $\mathbf{I}$  is the second order identity tensor,  $p$  is the pressure field.

*a. Initial and Boundary conditions* We set uniform values of velocity and pressure field throughout the domain as initial conditions. The boundary conditions are:

- Inlet: a time-varying paraboloid velocity profile whose cross-sectional average value is shown in Fig. 4 and has been obtained by digitizing the graph found in Philip et al<sup>4</sup> using an open-source application called *Engauge*. We use an 8-series Fourier decomposition for the average velocity, obtained using an in-built least-squares curve fitting algorithm available in MATLAB <sup>®</sup>, which is expressed as

$$v_{z,avg}(t) = a_0^v + \sum_{k=1}^8 \left[ a_k^v \cos\left(\frac{2\pi k}{T}t\right) + b_k^v \sin\left(\frac{2\pi k}{T}t\right) \right]$$

where  $T$  is the time-period of the cardiac cycle,  $a_0^v, a_k^v, b_k^v$  ( $k \in \{1, 2, \dots, 8\}$ ) are the corresponding Fourier components. Zero-gradient condition is used for pressure.

- Outlet: We impose a time-varying pressure as shown in Fig. 4 via 8-series Fourier decomposition for pressure. Zero-gradient condition is used for velocity.
- Endoluminal surface of AAA wall: No-slip condition is prescribed for velocity such that  $\mathbf{v} = \mathbf{0}$  while zero-gradient is used for the pressure field.

## B. Solid dynamical model for the Aneurysm wall

We model the AAA wall as linear elastic<sup>4,19</sup>, Saint Venant Kirchhoff elastic<sup>19,23</sup> as has been widely used in the literature. We also employ a non-linear isotropic phenomenological constitutive model for AAAs proposed by Raghavan et al.<sup>23</sup>. The model was obtained by performing nonlinear regression of experimental data, gathered from the mechanical testing of 69 human aneurysm tissue specimens subjected to uniaxial loading; we refer to this as Raghavan-Vorp elastic model. The mechanical properties of the AAA wall are assumed to be homogeneous: density  $\rho = 2000 \text{ kg/m}^3$  and material constants are as follows

- Linear elastic model:  $E = 2.7 \times 10^6 \text{ Pa}$ ,  $\nu^s = 0.45$ <sup>4,19</sup>

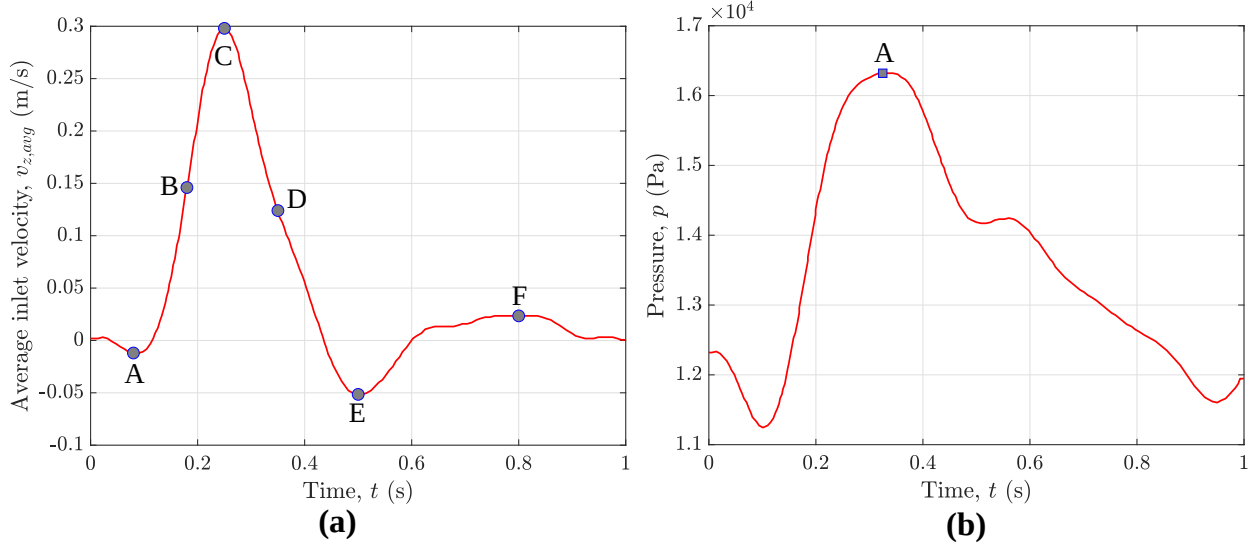


FIG. 4: Waveforms for (a) Average inlet velocity with markers indicating time instants: initiation of systole A ( $t = 0.08$  s), systolic acceleration B ( $t = 0.18$  s), peak systole C ( $t = 0.25$  s), systolic deceleration D ( $t = 0.35$  s), beginning of diastole E ( $t = 0.50$  s), late diastole F ( $t = 0.80$  s) (b) Outlet pressure with marker A ( $t = 0.32$  s) indicating peak pressure. Source: adapted from<sup>4</sup>

- Saint Venant Kirchhoff model:  $E = 2.7 \times 10^6$  Pa,  $\nu^s = 0.45$
- Raghavan-Vorp model<sup>23</sup>: material constants,  $\alpha = 1.74 \times 10^5$  Pa,  $\beta = 1.881 \times 10^6$  Pa,  $\nu^s = 0.45$

The wall thickness is considered to be uniform with a value of  $1.2 \text{ mm}^4$ .

We use total Lagrangian formulation of the governing equations for solid mechanics, where deformations and stresses are calculated with respect to the reference configuration, that is, the initial configuration of the solid. We represent the deformation by the deformation gradient tensor  $\mathbf{F}^{29,30}$  and the stress by the first Piola-Kirchhoff stress tensor  $\mathbf{P}$ .  $\mathbf{F}$  is expressed as function of the solid displacement  $\mathbf{u}$  as  $\mathbf{F} = \mathbf{I} + \nabla_0 \mathbf{u}$  where subscript 0 indicates differentiation with respect to the initial configuration. The balance of linear momentum for a deformable solid, neglecting body force, is

$$\rho_0^s \frac{\partial^2 \mathbf{u}}{\partial t^2} = \nabla_0 \cdot \mathbf{P} \quad (1)$$

The first and second Piola-Kirchhoff stress tensors<sup>30</sup>, denoted as  $\mathbf{P}$  and  $\mathbf{S}$  respectively, are related to each-other as  $\mathbf{P} = \mathbf{F} \cdot \mathbf{S}$  and the Cauchy stress tensor is related to  $\mathbf{P}$  and  $\mathbf{S}$

as<sup>30</sup>

$$\boldsymbol{\sigma}^s = \frac{1}{\det\{\mathbf{F}\}} \mathbf{P} \cdot \mathbf{F}^T = \frac{1}{\det\{\mathbf{F}\}} \mathbf{F} \cdot \mathbf{S} \cdot \mathbf{F}^T \quad (2)$$

The Green-Lagrange strain tensor is defined as

$$\mathbf{E} = \frac{1}{2} (\mathbf{F}^T \cdot \mathbf{F} - \mathbf{I}) = \frac{1}{2} \left( \underbrace{(\nabla_0 \mathbf{u} + (\nabla_0 \mathbf{u})^T)}_{\text{linear part}} + \underbrace{(\nabla_0 \mathbf{u})^T \cdot \nabla_0 \mathbf{u}}_{\text{non-linear part}} \right) \quad (3)$$

Now,  $\mathbf{E}$  is composed of linear as well as non-linear parts making it appropriate for measuring large deformations in elastic solids which shows a non-linear behaviour. A non-linear elastic model used to capture small strains and finite rotations is the Saint Venant-Kirchhoff model. For an isotropic material, the constitutive relation is given as

$$\mathbf{S} = 2\mu^s \mathbf{E} + \lambda^s \text{tr}(\mathbf{E}) \mathbf{I} \quad (4)$$

where  $\mu^s$  (also called shear modulus<sup>31</sup>) and  $\lambda^s$  are Lamé constants which are related to Young's modulus and Poisson ratio as<sup>32</sup>

$$\mu^s = \frac{E}{2(1 + \nu^s)} \text{ and } \lambda^s = \begin{cases} \frac{\nu^s E}{(1+\nu^s)(1-\nu^s)} & \text{plane stress} \\ \frac{\nu^s E}{(1+\nu^s)(1-2\nu^s)} & \text{plane strain and 3D cases} \end{cases} \quad (5)$$

*a. Linear elastic model* Under the assumption of small deformations and small rotations, the non-linear term will be very small compared to the linear terms and thus can be neglected. This would result in Cauchy infinitesimal strain tensor<sup>33</sup> defined as  $\boldsymbol{\epsilon} = \frac{1}{2} (\nabla_0 \mathbf{u} + (\nabla_0 \mathbf{u})^T)$ . Also, the second Piola-Kirchhoff stress tensor  $\mathbf{S}$  reduces to Cauchy stress tensor  $\boldsymbol{\sigma}$  and the constitutive relation is the isotropic Hooke's law

$$\boldsymbol{\sigma}^s = 2\mu^s \boldsymbol{\epsilon} + \lambda^s \text{tr}(\boldsymbol{\epsilon}) \mathbf{I} \quad (6)$$

*b. Raghavan-Vorp elastic model* Raghavan et al.<sup>23</sup> obtained the following constitutive equation relating the Cauchy stress tensor and the elastic deformation

$$\boldsymbol{\sigma}^s = -p \mathbf{I} + 2[\alpha + 2\beta(I_b - 3)] \mathbf{b} \quad (7)$$

where  $p$  is the Lagrange multiplier to enforce incompressibility,  $\alpha$  and  $\beta$  are material constants obtained after fitting uniaxial loading experimental data to the proposed model,  $\mathbf{b} = \mathbf{F} \mathbf{F}^T$  is left Cauchy-Green tensor and  $I_b$  is its first principal invariant. Since arterial

wall is nearly (but not exactly) incompressible, we developed a weakly compressible version of Raghavan-Vorp model for which the constitutive relation is given as

$$\boldsymbol{\sigma}^s = \frac{\kappa}{2} \left( J - \frac{1}{J} \right) \mathbf{I} + \text{dev} \left( \frac{2}{J} \left[ \alpha + 2\beta(I_{\bar{\mathbf{b}}} - 3) \right] \bar{\mathbf{b}} \right) \quad (8)$$

where  $\bar{\mathbf{b}} = J^{-2/3} \mathbf{b}$  ( $J = \det\{\mathbf{F}\}$ ) and  $\kappa = \frac{2}{3}\mu^s + \lambda^s$

From Eqn. 2, we have

$$\boldsymbol{\sigma}^s = \frac{1}{J} \mathbf{P} \cdot \mathbf{F}^T \implies \mathbf{P} = J \boldsymbol{\sigma}^s \mathbf{F}^{-T} \quad (9)$$

Using Eqns. 9 and 8 in Eqn. 1, we obtain the governing equation for Raghavan-Vorp elastic material which is solved to obtain the solid displacement field  $\mathbf{u}$ .

*c. Initial and Boundary conditions (BCs)* The governing equations for solid domain are solved for displacement field. We set the displacement and velocity fields to be zero throughout the domain as initial conditions. We impose zero displacement conditions,  $\mathbf{u} = \mathbf{0}$ , at the extremities or side faces. The internal (endoluminal) surface is subjected to Neumann boundary conditions which is the time-varying pressure loading  $p$  corresponding to the cardiac cycle (Fig. 4). The external surface is traction-free.

### C. Simulation setup

We have the following expression for the idealized fusiform AAA lumen geometry in terms of the maximum AAA diameter  $D_{max}$ , proximal neck diameter  $D_{neck2}$  and height of the aneurysm sac  $H$  as

$$r(z) = \left( \frac{D_{max} - D_{neck2}}{4} \right) \left[ 1 + \sin \left( \frac{2\pi z}{H} - \frac{\pi}{2} \right) \right] + \frac{D_{neck2}}{2} \quad ; \quad 0 \leq z \leq H$$

It is also assumed that the proximal and distal neck diameters are equal  $D_{neck1} = D_{neck2}$ . We take  $D_{max} = 5$  cm.

*a. Simulation domain* For proper imposition of inlet and outlet boundary conditions, it is advised in the literature<sup>4,19,34</sup> to extend the inlet and outlet faces of the AAA by some multiples of the corresponding face diameters. We infer from the schematic of AAA (see Fig. 1), that the branching of the abdominal aortic proximal and distal to AAA would have a strong influence on the blood flow dynamics in both neck regions and taking longer extensions would be unreasonable. Therefore, both inlet and outlet extensions are taken to be  $2D_{neck2}$ .

We used an open-source computer-aided design (CAD) software *Salome*<sup>35</sup> for preparing the AAA lumen geometries. The schematic of the AAA geometry is shown in Fig. 5. We used a fine mesh comprising of prism layers to properly resolve the unsteady boundary layer at the wall for fluid domain and capture flow dynamics accurately. As suggested in Krishna et al.<sup>34</sup>, boundary layer thickness  $\delta$  for oscillatory flows is of the order  $\delta \sim \sqrt{\nu^f T}$ , where  $\nu^f = \frac{\mu^f}{\rho^f}$  is the kinematic viscosity of the blood and  $T$  is the time-period of the cardiac cycle. Using the blood properties, we obtain

$$\delta \approx \sqrt{\frac{0.0044}{1050} \cdot 1} = 2 \times 10^{-3} \text{ m}$$

implying that the fluid mesh ought to be refined upto a distance of  $2 \times 10^{-3}$  m from the wall.

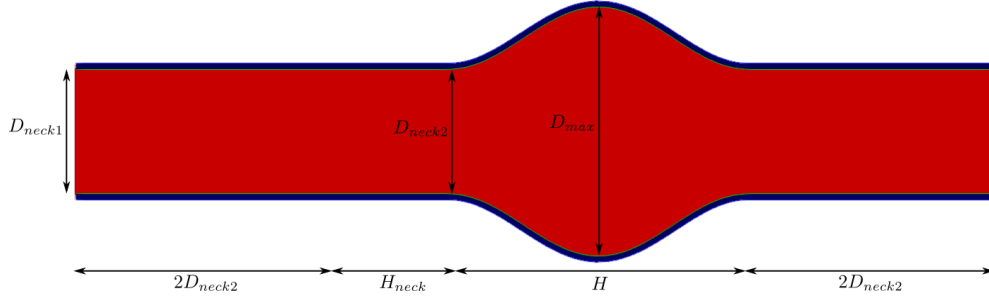


FIG. 5: Idealized fusiform AAA geometry for simulation

An open-soure mesh generation tool called *cfMesh*<sup>36</sup> was used to generate fluid mesh for the AAA lumen (Fig. 6a). On the other hand, the solid mesh for each AAA geometry was generated by extruding the wall patch of the fluid mesh using *extrudeMesh* along the local wall-normal direction for a prescribed normal height which happens to be the uniform wall thickness of the AAA, and number of layers (Fig. 6b). We use an open-source package called *solids4Foam* which can be installed on the top of *foam-extend 4.0*, a branch of the widely known software for CFD simulations called OpenFOAM. It provides a host of applications (solvers and utilities) to deal with a wide variety of problems in fluid dynamics, solid dynamics and fluid-structure interactions.

#### D. Hemodynamic and arterial wall stress parameters

For analyzing the blood flow in the AAAs, we consider the variation of wall shear stress (WSS) and its derived quantities. We also study vortex dynamics and identify the vortical

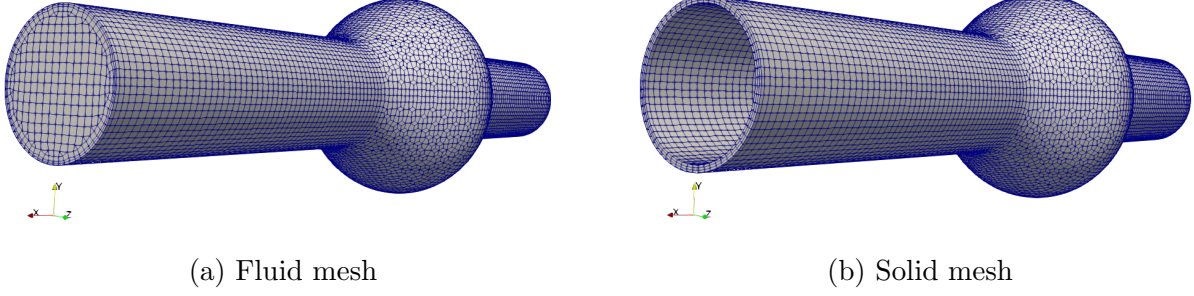


FIG. 6: Computational mesh for (a) fluid and (b) solid domains

(coherent) structures using  $\lambda_2$ -criterion<sup>37,38</sup>, a velocity gradient-based vortex identification method. To assess stress in the arterial wall, we use von Mises stress and first principal stress.

*a. Wall shear stress* Wall shear stress (WSS) vector  $\boldsymbol{\tau}_w$  is defined as the tangential component of the traction vector  $\boldsymbol{t}$  at the wall. Traction vector is obtained as  $\boldsymbol{t} = \boldsymbol{\sigma}^f \cdot \boldsymbol{n}^f$ , where  $\boldsymbol{\sigma}^f$  is Cauchy stress tensor and  $\boldsymbol{n}^f$  is the wall normal unit vector. WSS vector<sup>39</sup> is obtained as  $\boldsymbol{\tau}_w = \boldsymbol{t} - (\boldsymbol{t} \cdot \boldsymbol{n}^f) \boldsymbol{n}^f$ . We look at the following derived quantities to get a holistic view of the wall shear stress<sup>4,40–42</sup>:

- Time-averaged wall shear stress (*TAWSS*) is calculated as  $TAWSS(\boldsymbol{x}) = \frac{1}{T} \int_0^T \|\boldsymbol{\tau}_w(\boldsymbol{x}, t)\| dt$
- Oscillatory shear index (*OSI*) is a dimensionless metric which characterises whether the WSS vector is aligned with the *TAWSS* vector throughout the cardiac cycle,  $OSI(\boldsymbol{x}) = \frac{1}{2} \left( 1 - \frac{\|\frac{1}{T} \int_0^T \boldsymbol{\tau}_w(\boldsymbol{x}, t) dt\|}{\frac{1}{T} \int_0^T \|\boldsymbol{\tau}_w(\boldsymbol{x}, t)\| dt} \right)$
- Spatial gradient of the mean wall shear stress (*WSSG<sub>S</sub>*) is calculated as  $WSSG_S = \|\nabla(\text{meanWSS})\|$
- Peak systole wall shear stress,  $PSWSS(\boldsymbol{x}) = \|\boldsymbol{\tau}_w(\boldsymbol{x}, t_{ps})\|$  where  $t_{ps}$  is the time instant of peak systole

*b. Arterial wall stress* The state of stress at every material point in the arterial wall is defined in terms of Cauchy stress tensor  $\boldsymbol{\sigma}^s$  which is symmetric and consists of 6 components, namely,  $\sigma_{ij}^s$  ( $i, j = x, y, z$ ). We quantify the stress state at every point in terms of von Mises stress and maximum principal stress  $\sigma_1$ . The von Mises stress  $\sigma_{eq}$  is defined as

$$\sigma_{eq} = \frac{1}{\sqrt{2}} \sqrt{(\sigma_{xx} - \sigma_{yy})^2 + (\sigma_{yy} - \sigma_{zz})^2 + (\sigma_{xx} - \sigma_{zz})^2 + 6(\sigma_{xy}^2 + \sigma_{yz}^2 + \sigma_{xz}^2)}$$

while the maximum principal stress  $\sigma_1$  is the maximum eigenvalue of  $\boldsymbol{\sigma}^s$ .

### III. HEMODYNAMICS SIMULATIONS OF AAA LUMEN GEOMETRIES

We perform hemodynamic simulations assuming the AAA vessel walls to be rigid using Newtonian and Carreau-Yasuda constitutive models for blood. At first, we do a comparative study of the effect of constitutive models on the hemodynamics within AAA1 is analyzed with special emphasis on wall shear stress (WSS) and other derived quantities –  $PSWSS$ ,  $meanWSS$ ,  $WSSG_S$ ,  $TAWSS$ ,  $OSI$ . Thereafter we examine the role played by DHr on the flow dynamics within AAA1 and AAA2.

We carry out the simulations for 4 cardiac cycles since the distinction between solutions corresponding to two consecutive cycles after the second cycle were indistinguishable implying periodicity in solution. We perform a mesh convergence study for AAA1 using three meshes with the number of cells increasing progressively with a factor of approximately 2 as tabulated in Table I. The time-step size is also progressively decreased by a factor of 2 such that a constant maximum Courant-Friedrichs-Levy (CFL) number of 1, that is  $CFL \leq 1$ , is maintained throughout every simulation.

	Coarse	Medium	Fine
Number of cells (in millions)	1.82	3.66	6.8
Number of prismatic layers at the wall	5	9	12
Time-step size (in seconds)	$2 \times 10^{-4}$	$1 \times 10^{-4}$	$5 \times 10^{-5}$

TABLE I: Simulation details

We observe negligible difference in  $SWSS$  amongst the results obtained for the meshes. Therefore, we choose the medium mesh for further analysis.

#### A. Effect of blood constitutive models: Carreau-Yasuda versus Newtonian

The axial velocity ( $v_z$ ) contours plotted at different stations along AAA1 lumen (Fig. 7) for the time instants marked in Fig. 4(a) suggest that  $v_z$  at the central portion of each station is higher for the Newtonian model than for the Carreau-Yasuda model throughout the cardiac cycle. This is consistent with the fact that dynamic viscosity  $\mu^f$  is higher in the regions facing lower shear rate, which typically occurs in the core of the flow, and thus

decelerating the flow in those areas.

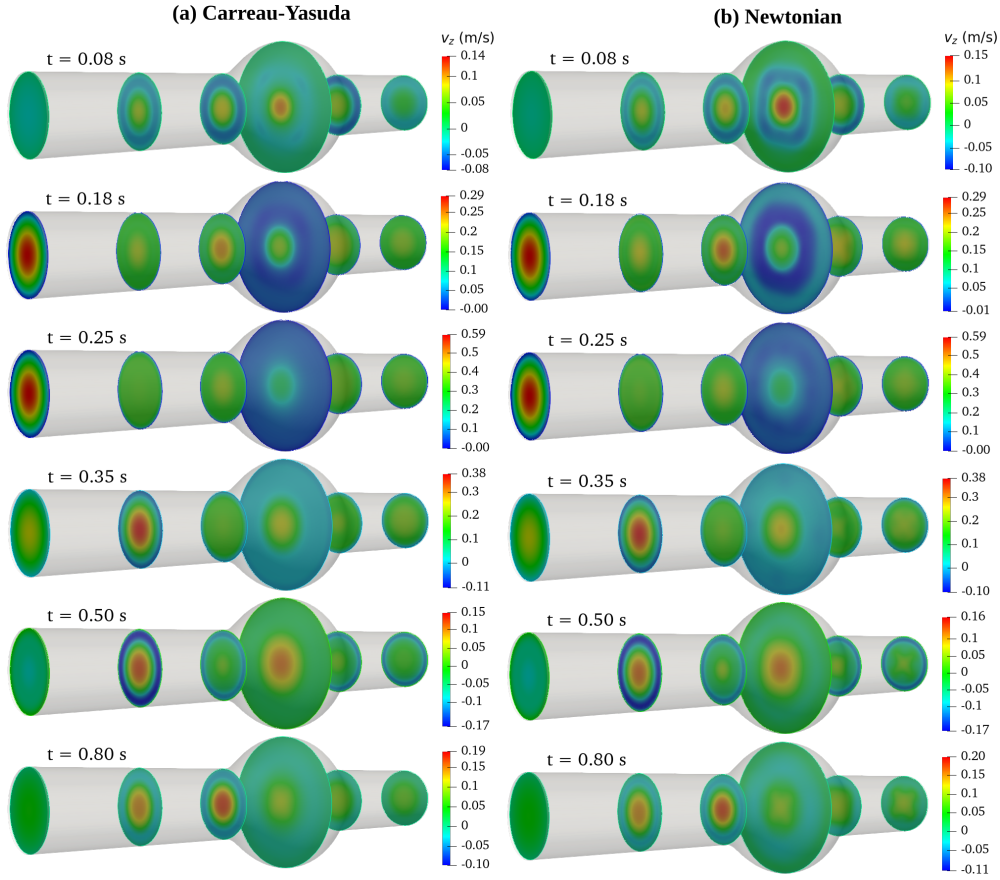


FIG. 7: Velocity contours at different stations: (a) Carreau-Yasuda and (b) Newtonian models

### 1. Vortex dynamics

A presentation of vortex dynamics in Fig. 8(a) displays strong correlation between the regions of high values of vorticity  $\omega$  ( $= \nabla \times \mathbf{v}^f$ ) and ring vortices obtained using  $\lambda_2$ -criterion for a fixed  $\lambda_2 = -75 \text{ s}^{-1}$  for Carreau-Yasuda model. As has been discussed in Finol et al.<sup>5,13</sup>, the growth, decay and transport of vortices in the flow can be divided into the following flow phases alongwith the corresponding time intervals in the cardiac cycle

- *Systolic acceleration* ( $t = 0.08 \text{ s}$  to  $t = 0.25 \text{ s}$ ) involves downstream transport of the residual vortices, left from the previous cardiac cycle, out of the aneurysms, resulting in a completely attached flow pattern.

- *Systolic deceleration* ( $t = 0.25$  s to  $t = 0.50$  s) is characterized by flow separation at the proximal neck of the aneurysm, the growth of a single-vortex near the midsection which then moves downstream.
- *Early diastole* ( $t = 0.50$  s to  $t = 0.85$  s) involves gradual weakening of the vortex shed at the end of systole as it translates downstream and the growth of the translating single-vortex.
- *Late diastole* ( $t = 0.85$  s to  $t = 0.08$  s) is the interval where the most significant flow disturbance takes place, mainly due to the low-velocity recirculation region inside the aneurysm towards its distal end. Also, the downstream vortex translation leads to enclosing of the forward flow stream by the vortex.

The vortex dynamics for Newtonian case differs slightly from that of the Carreau-Yasuda in that there is an occurrence of a weak wavy-like ring vortex of large diameter in all but systolic deceleration phase as seen in Fig. 8(a) and (b).

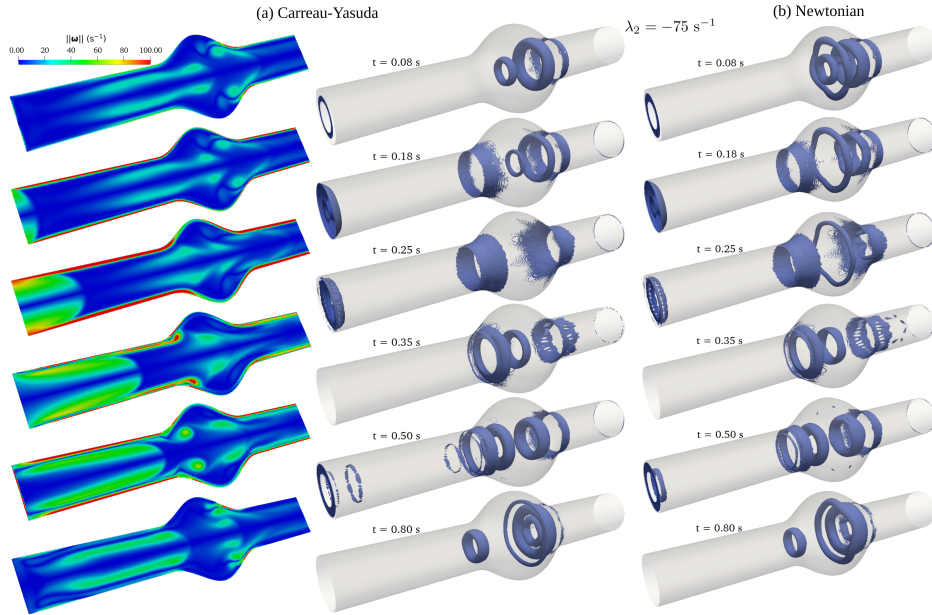


FIG. 8: Vortex dynamics: (a) Vorticity contours and  $\lambda_2 = -75 \text{ s}^{-1}$  iso-surface for Carreau-Yasuda model, (b)  $\lambda_2 = -75 \text{ s}^{-1}$  iso-surface for Newtonian model.

## 2. *WSS and derived quantities*

We learn from Fig. 9a that *PSWSS* values for Newtonian case are higher than the Carreau-Yasuda case throughout the domain and the difference is prominently noticeable in the portion towards the distal end of the aneurysm sac; the maximum *PSWSS* values reaching 3.19 Pa and 3.01 Pa respectively. This is so because the dynamic viscosity is lower in the wall region for the Carreau-Yasuda case which produces lower wall shear stress.

Like *PSWSS*, Newtonian model overpredicts *TAWSS* compared to Carreau-Yasuda model (see Fig. 9b) with higher variations in the distal region of the aneurysm. While the maximum *TAWSS* in the case of Carreau-Yasuda model reaches 0.9 Pa, the corresponding value for Newtonian model is 1.04 Pa; an increase of 16%.

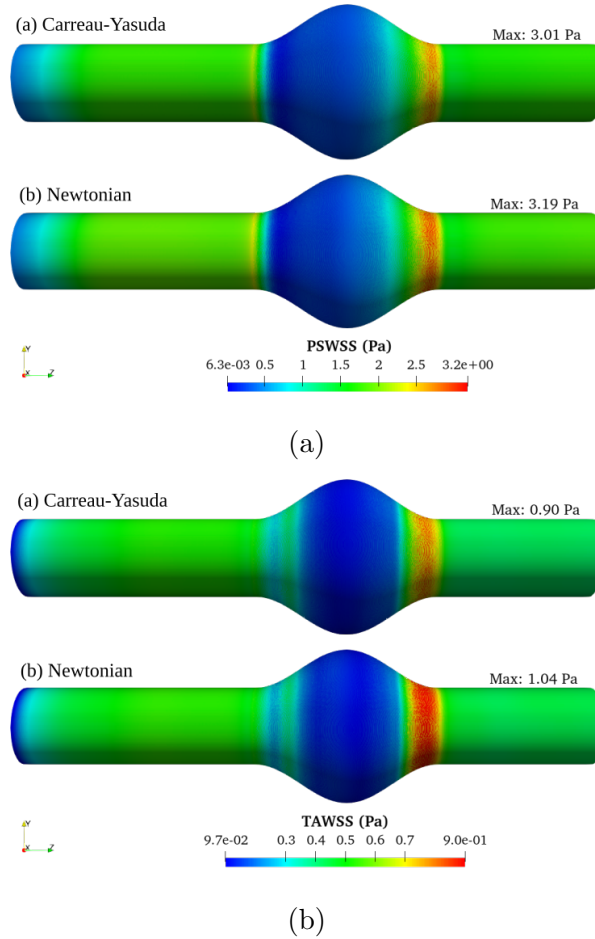


FIG. 9: (left) *PSWSS* and (right) *TAWSS* distributions for (a) Carreau-Yasuda and (b) Newtonian models for AAA1

We observe from Fig. 10 that blood flow undergoes higher fluctuations in the aneurysm sac for Carreau-Yasuda case than when the blood is assumed to be Newtonian. It is also noticed that while high  $OSI$  values are found in the central portion of the aneurysm sac, the high  $OSI$  region forming a narrow band shifts proximally in the Newtonian case.

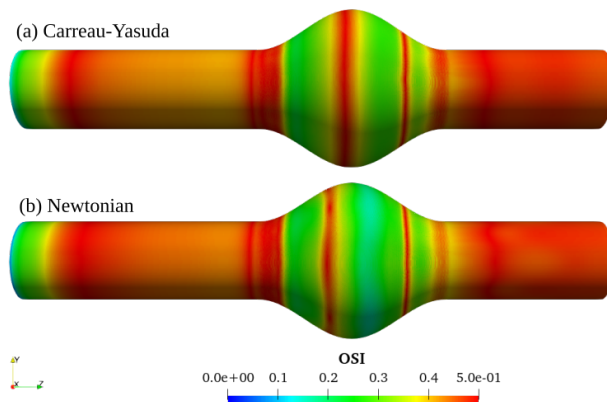


FIG. 10:  $OSI$  distribution: (a) Carreau-Yasuda and (b) Newtonian models

## B. Effect of DHr: AAA1 versus AAA2

We study how the flow dynamics is influenced by the shape index DHr - AAA1 with a higher DHr and AAA2 with a lower DHr. For both cases, simulations have been performed using Carreau-Yasuda blood model.

### 1. Velocity contours

Fig. 11 shows the axial velocity ( $v_z$ ) contours plotted at different stations along AAA2 lumen for various time instants. The velocity at the maximum bulge location is relatively lower than other stations for all time instants but  $t = 0.5$  s.

The flow dynamics inside AAA1 forms larger recirculation zones and flow separation than that of AAA2. The difference in the extent of recirculation regions are conspicuous at  $t = 0.08, 0.18, 0.8$  s. In such regions, thrombus finds a fertile environment to settle down and gradually increase in size. Therefore, there is an increased chance of ILT deposition in AAA1 compared to AAA2, as has been suggested in Philip et al.<sup>4</sup>.

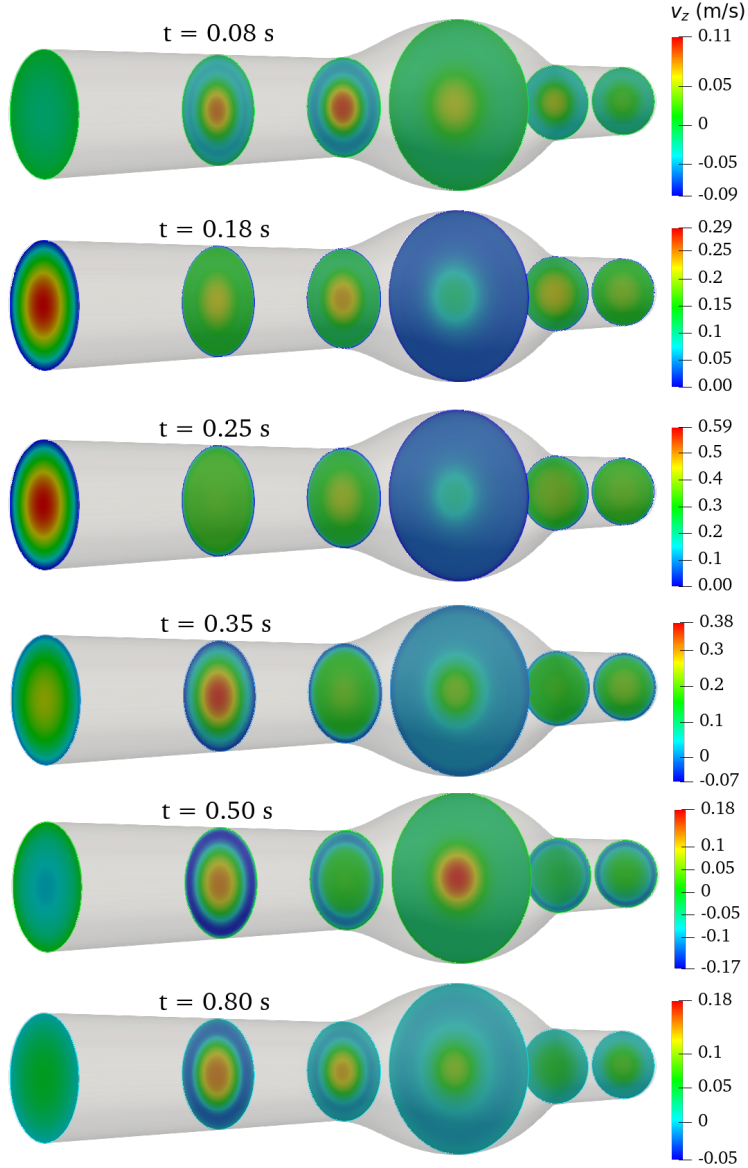


FIG. 11: Velocity contours at different stations of AAA2

## 2. *Pressure contours*

We observe from Fig. 13 that the temporal acceleration and deceleration of the flow has a major influence on the pressure distribution throughout the cardiac cycle in both AAAs. The flow sees strong favourable pressure gradient in the initial systolic phase, that is, between  $t = 0.1$  s to  $t = 0.25$  s. For the remaining interval of the cardiac cycle, the flow suffers from adverse pressure gradient and is strongest somewhere around  $t = 0.35$  s.

The pressure distribution for AAA1 and AAA2 appears to remain fairly similar except for symmetric pockets of lower pressure found in the aneurysm sac of AAA1 at  $t = 0.08$  s,

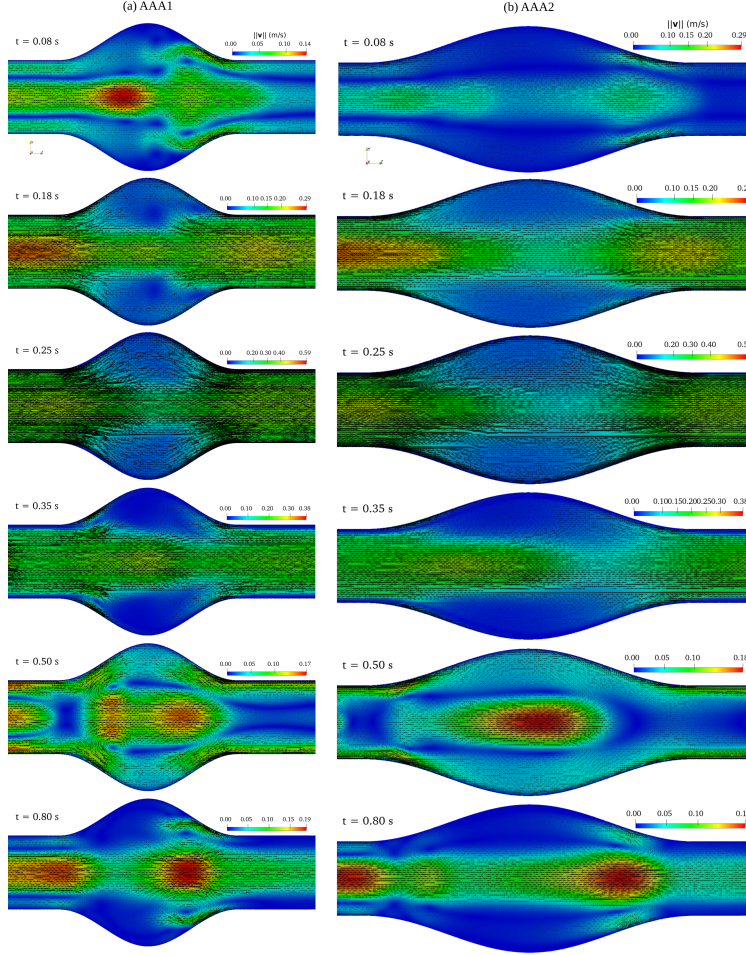


FIG. 12: Velocity vector plot in the longitudinal plane of the aneurysm sac: (a) AAA1 (b) AAA2

$t = 0.5$  s and  $t = 0.8$  s which are absent in AAA2. These pockets can be correlated with ring vortices formed in AAA1. Our results are consistent with the findings of Finol et al.<sup>12</sup>.

### 3. Vortex dynamics

The vortex dynamics for AAA2 can be categorised into the same flow phases that were discussed earlier in Section III A 1 and display similar behaviour. For  $\lambda_2 = -75 \text{ s}^{-1}$  iso-surface shown in Fig. 14, we note the following distinctions pertaining to the vortex dynamics in the flow phases of AAA1 and AAA2

- *Systolic acceleration* ( $t = 0.08$  s to  $t = 0.25$  s): A weak vortex is observed at the distal end of AAA2 unlike two vortices found at the mid-way and distal end of AAA1 sac.

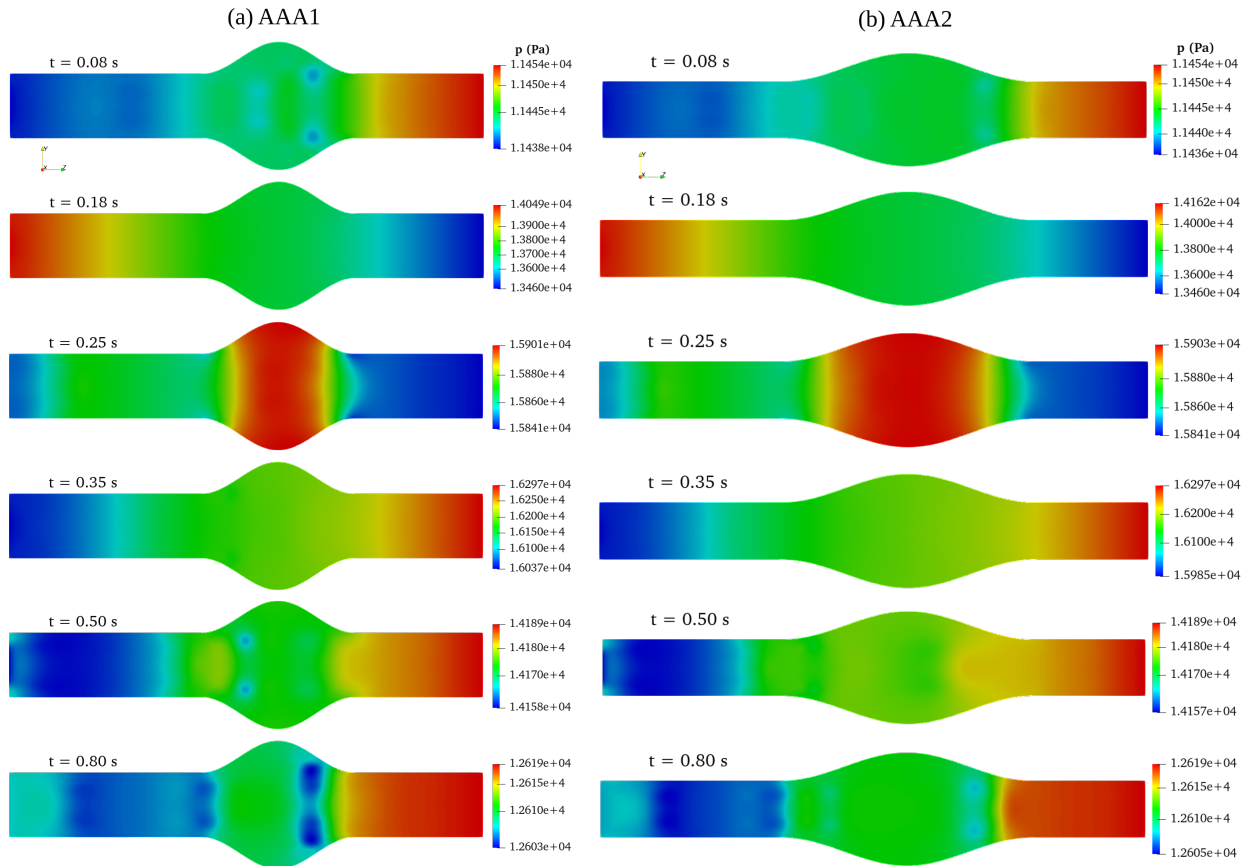


FIG. 13: Pressure distribution in the longitudinal plane for (a) AAA1 and (b) AAA2

In both, the vortices continue to decay till they vanish at peak systole.

- *Systolic deceleration* ( $t = 0.25$  s to  $t = 0.50$  s): The growth of two vortices formed at the proximal end and mid-way of AAA1 sac takes place; both translates downstream. A weak vortex forms in the proximal end of AAA2 sac which moves downstream too.
- *Early diastole* ( $t = 0.50$  s to  $t = 0.85$  s): While significant flow disturbance takes place in AAA1 causing growth, decay and translation of multiple vortices, the situation in AAA2 is relatively quiet.

The gradual weakening of the vortex shed at the end of systole as it translates downstream and the growth of the translating single-vortex.

- *Late diastole* ( $t = 0.85$  s to  $t = 0.08$  s): The downstream vortex translation leads to enclosing of the forward flow stream by the vortex in AAA1. However, decay of two vortices at the proximal end of AAA2 takes place accompanied by a gradual narrowing

of the distal vortex.

In a nutshell, AAA1 has richer and more proactive vortex dynamics than AAA2.

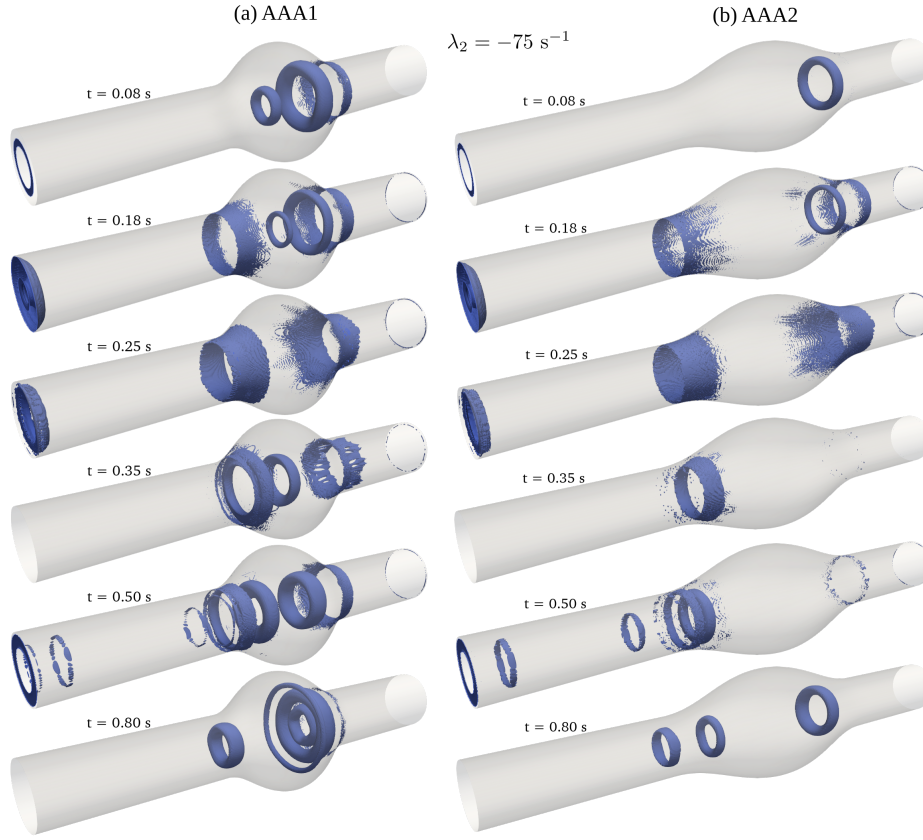


FIG. 14: Vortex dynamics:  $\lambda_2 = -75 \text{ s}^{-1}$  iso-surface contours for (a) AAA1 (b) AAA2.

#### 4. *WSS and derived quantities*

$PSWSS$  varies from 0.0093 to 3 Pa in the case of AAA1 and 0.33 to 2.3 Pa for AAA2 (Fig. 15). In both the cases, the maximum  $PSWSS$  occurs at the corresponding distal ends.

It can be observed Fig. 15 that while  $TAWSS$  varies from 0.097 to 0.9 Pa in AAA1, AAA2 sees a variation in the range 0.11 to 0.53 Pa. AAA1 sees lower values of  $TAWSS$  than AAA2 in the region left to its maximum bulge. In either cases, we find that coexisting high and low  $TAWSS$  regions persists towards the proximal end (and even at the distal end) creating a fertile ground for the thrombus formation inside the AAAs<sup>16</sup>. This is more apparent in AAA1 case.

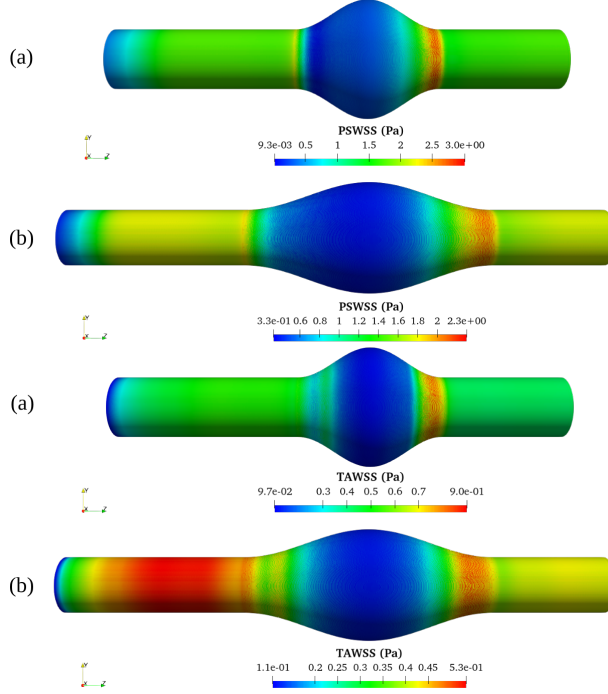


FIG. 15:  $PSWSS$  and  $TAWSS$  distributions for (a) AAA1 and (b) AAA2

AAA1 suffers from higher maximum  $WSSG_S$  (value being 203.1 Pa/m) than AAA2 (value is 85.10 Pa/m); an increase by a factor of 2 than AAA2 (Fig. 16). In either case, the maximum happens to be located at the proximal and distal ends. The high  $OSI$  region in the central portion of AAA1, flanked by lower  $OSI$  regions on either sides (Fig. 16), suggests that the flow velocity undergoes severe fluctuations for the maximum bulge location. However, the situation is quite different for AAA2 in which  $OSI$  progressively increases from its proximal end to its distal end.

#### IV. COMPUTATIONAL SOLID STRESS SIMULATIONS OF ARTERIAL WALL MECHANICS

We perform transient solid mechanics or computational solid stress ( $CSS_T$ ) simulations for both AAA1 and AAA2 walls. In  $CSS_T$ , a time-varying uniform pressure loading corresponding to the cardiac cycle (see Fig. 4) is applied on the endoluminal surface of the aneurysmal walls. We study the influence of solid material materials and  $DHr$  on the wall mechanics.

We consider three different mesh resolutions for AAA1 wall using time-step size of  $5 \times 10^{-3}$

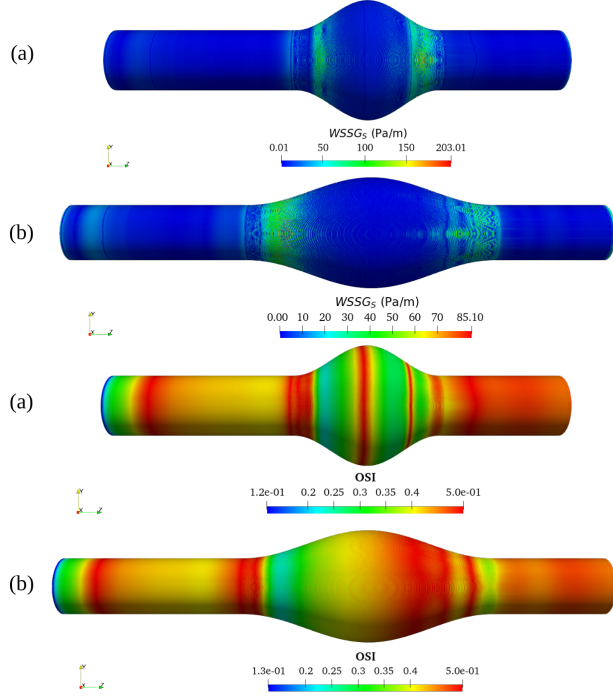


FIG. 16:  $WSSG_S$  and  $OSI$  distributions for (a) AAA1 and (b) AAA2

s. Although the governing equations for solid dynamics use total Lagrangian formulation, we still allow the simulation to run for two cardiac cycles to achieve solution periodicity.

	Number of cells in radial direction	Number of cells
Coarse	3	31,500
Medium	5	73,800
Fine	8	1,63,700

TABLE II: Mesh information

It can be inferred from Fig. 17a that there is negligible difference between the maximum von Mises stress corresponding to the medium and fine meshes.

For the medium mesh, we consider three time-step sizes for time integration, namely,  $5 \times 10^{-3}$  s,  $2.5 \times 10^{-3}$  s and  $1.0 \times 10^{-3}$  s. We infer from Fig. 17b that the influence of time-step size on the solution, here maximum von Mises stress in the wall, is negligible.

On the basis of spatial and temporal convergence studies, we choose the medium mesh for further simulations on AAA1 wall using a time-step of  $2.5 \times 10^{-3}$  s. The mesh settings

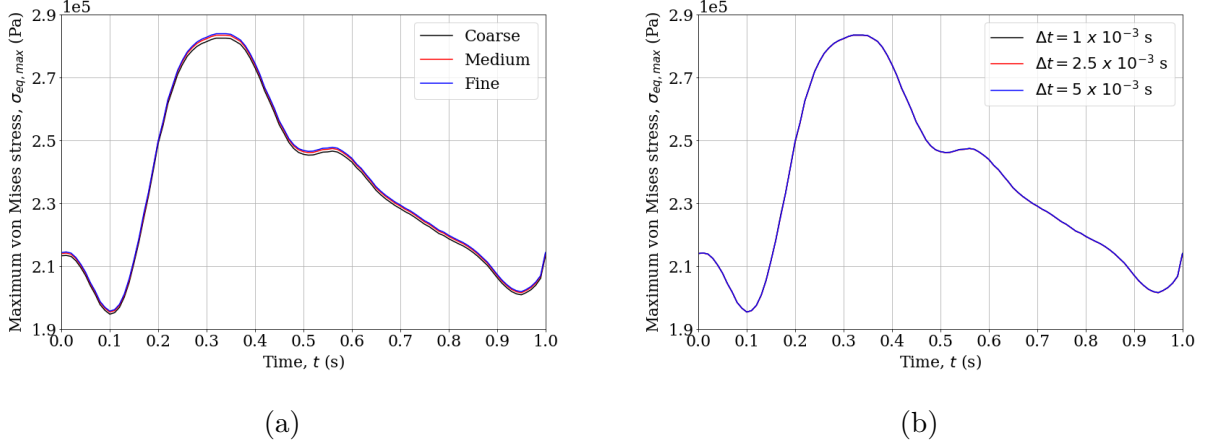


FIG. 17: AAA1 wall modeled as a linear elastic material: (a) Mesh and (b) Temporal convergence

utilised to discretise AAA1 wall is used for AAA2 wall as well.

### A. Influence of solid material models and DHr

Fig. 18a shows the total displacement  $\|\mathbf{u}\|$ , von Mises stress  $\sigma_{eq}$  and the first principal stress  $\sigma_1$  for AAA1 wall modeled as Raghavan-Vorp elastic model at  $t = 0.32$  s, that is the peak time of the uniform pressure loading. The displacement is highest (2.98 mm) in the midway of the initiation of curvature and the maximum bulge location. A similar observation is made regarding  $\sigma_{eq}$  and  $\sigma_1$  whose maximum values are  $3.62 \times 10^5$  Pa and  $3.90 \times 10^5$  Pa respectively. The region flanking the central portion of the bulge sees reduced values for all these variables. The maximum displacement is about 3.37 mm for AAA2 wall (see Fig. 18b), higher than the corresponding value for AAA1 wall. Likewise, the peak values for  $\sigma_{eq}$  and  $\sigma_1$  are  $3.35 \times 10^5$  Pa and  $3.70 \times 10^5$  Pa respectively, lower than the corresponding values for AAA1 wall. Since the peak wall stress is higher in the case of AAA1, this keeps it at a higher risk of rupture than AAA2.

Our  $\sigma_1$  results lie within the range as obtained by Perez et al.<sup>21</sup> who performed a steady state FEM analysis conducted on 190 AAA geometries with the endoluminal surface of the AAAs subjected to uniform peak pressure of the cardiac cycle and obtained an average maximum  $\sigma_1$  to be  $5.6 \times 10^5$  Pa ( $2.2 \times 10^5 - 1.18 \times 10^6$  Pa).

Since the trend of variation of  $\|\mathbf{u}\|$ ,  $\sigma_{eq}$  and  $\sigma_1$  differ only quantity-wise for each material

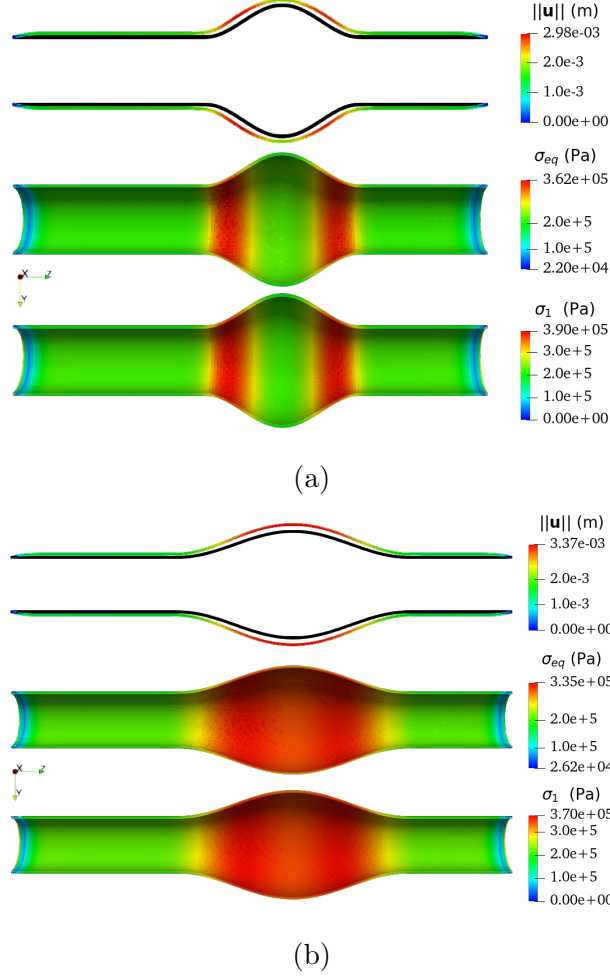


FIG. 18: Total displacement (top), von Mises stress (middle), first principal stress (bottom) for (a) AAA1 and (b) AAA2 walls modeled as Raghavan-Vorp elastic material at  $t = 0.32$  s under peak uniform pressure loading

model but not quality-wise, we shall plot the peak values of these quantities over a cardiac cycle for both AAA1 and AAA2 cases.

### 1. Influence of constitutive models for solid

The maximum displacement of the AAA1 wall in the case of Raghavan-Vorp elastic model (value is  $\approx 3$  mm) is about 1.4 times that of linear elastic (value is  $\approx 2.1$  mm) and approximately 1.8 times that of Saint Venant Kirchhoff elastic models (Fig. 19). Maximum von Mises stress in AAA1 wall for Raghavan-Vorp elastic model ( $\approx 3.60 \times 10^5$  Pa) is 12.4 % higher than the corresponding value of Saint Venant Kirchhoff and 28 % higher than the

linear elastic models (Fig. 20a). Similarly, maximum first principal stress for Raghavan-Vorp model ( $\approx 3.90 \times 10^5$  Pa) is 11.4 % and 18.2 % higher than the Saint Venant Kirchhoff and linear elastic models (Fig. 20b). A particular thing to note is that while maximum  $\sigma_{eq}$  and  $\sigma_1$  is higher for Saint Venant Kirchhoff model as compared to linear elastic case, it is the otherwise for  $\|\mathbf{u}\|_{max}$ .

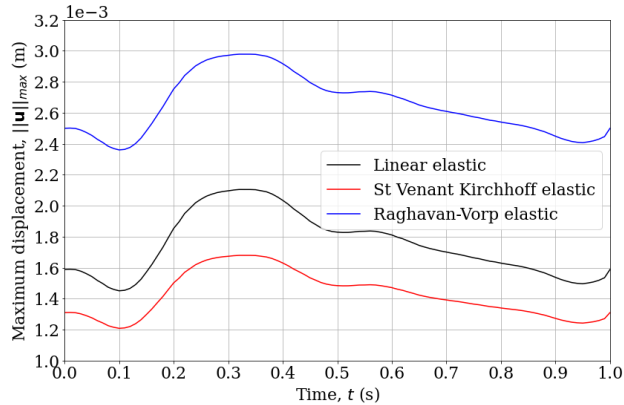


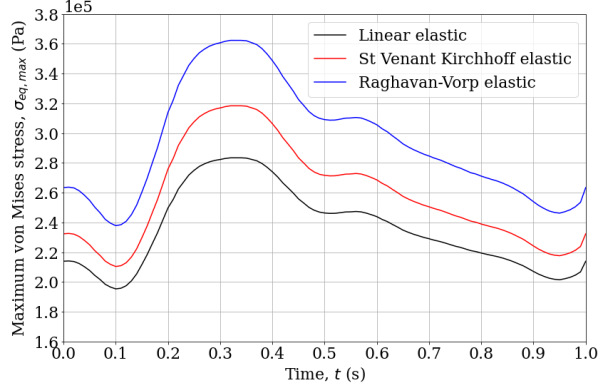
FIG. 19: Variation of maximum total displacement in AAA1 wall over a cardiac cycle for linear, Saint Venant Kirchhoff and Raghavan-Vorp elastic models

## 2. Influence of $DHr$

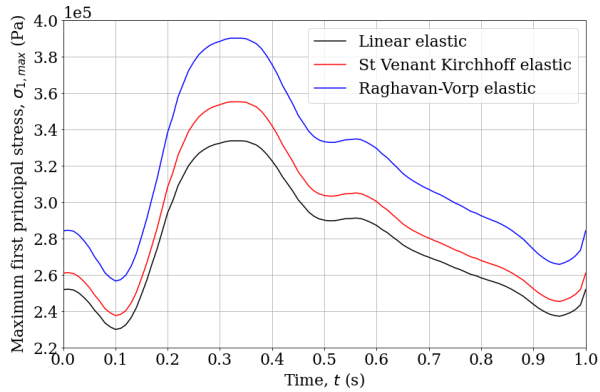
Since we have already observed how material model influences the wall mechanics, we shall now consider the results when the AAA1 and AAA2 walls are modeled using the more realistic Raghavan-Vorp elastic model.  $\|\mathbf{u}\|_{max}$  of the AAA2 wall (value is  $\approx 3.4$  mm) is about 13.3 % higher than that of AAA1 wall (value is  $\approx 3.0$  mm) (see Fig. 21). Maximum  $\sigma_{eq}$  in AAA1 wall ( $\approx 3.60 \times 10^5$  Pa) is 7.5 % higher than the corresponding value of AAA2 wall (Fig. 22a). Likewise, maximum  $\sigma_1$  of AAA1 case ( $\approx 3.90 \times 10^5$  Pa) is 5.4 % higher than that of AAA2 (Fig. 22b).

## V. CONCLUSION

In this paper, we have investigated the role of hemodynamic parameters and maximum wall stress in assessing rupture risk of abdominal aortic aneurysms (AAAs) which are local dilatations in the abdominal aorta in the infrarenal segment. Patient-specific AAAs can



(a)



(b)

FIG. 20: Variation of (a) maximum principal stress and (b) maximum von Mises stress in AAA1 wall over a cardiac cycle for linear, Saint Venant Kirchhoff and Raghavan-Vorp elastic models

be characterised by certain shape indices derived from geometrical parameters, such as maximum transverse diameter, neck diameters, abdominal height, bulge height. One shape index which is found to influence AAA biomechanics significantly is the ratio of maximum transverse diameter to abdominal height, also called, DHr. AAA biomechanics for two AAA geometries, AAA1 and AAA2 of different DHr (AAA1 has higher DHr) is investigated in detail with the help of uncoupled hemodynamics and AAA wall mechanics simulations. Blood is modeled as a Newtonian fluid and a non-Newtonian Carreau-Yasuda fluid. The vortex dynamics is quite similar for both the models, except for the presence of weak ring vortices in the Newtonian case. It is found that Newtonian case overpredicts WSS and time-averaged WSS (*TAWSS*) throughout the aneurysm sac, primarily in the distal end, and has lower

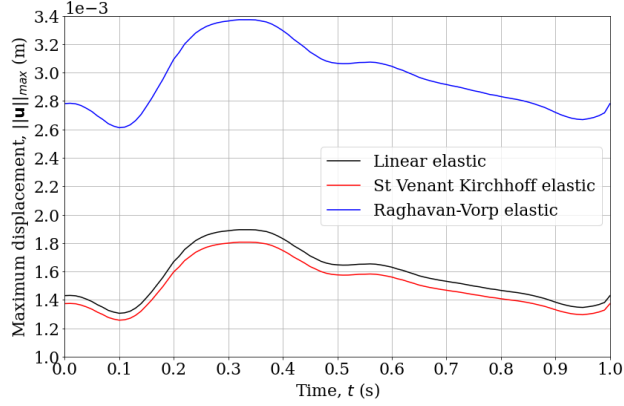


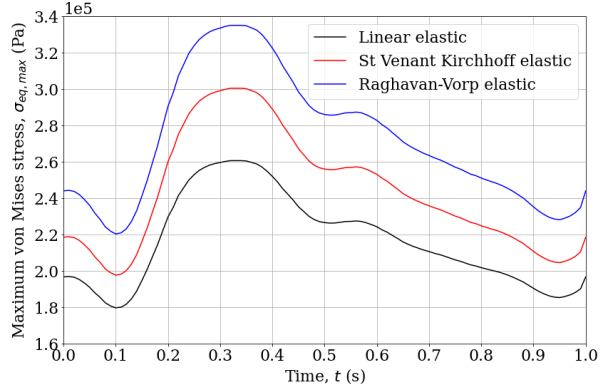
FIG. 21: Variation of maximum total displacement in AAA2 wall over a cardiac cycle for linear, Saint Venant Kirchhoff and Raghavan-Vorp elastic models

WSS fluctuations leading to lower oscillatory shear index ( $OSI$ ). The flow inside AAA1 forms larger recirculation regions and has richer vortex dynamics than AAA2. The former also has lower  $TAWSS$  and higher  $OSI$  in its proximal end alongwith higher WSS spatial gradient  $WSSG_S$  than AAA2. All these factors point to an increased susceptibility to thrombus deposition in the case of AAA1 which is a major predisposing factor for AAA rupture.

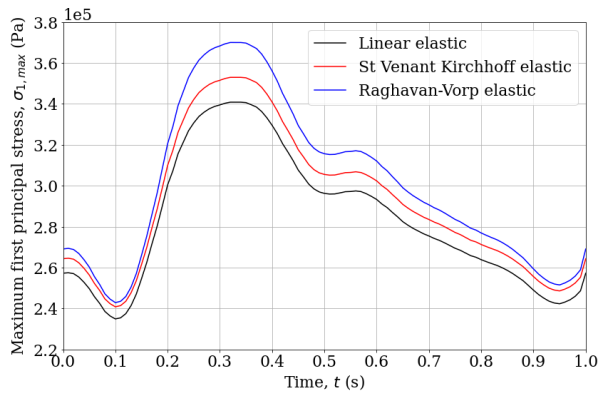
Three constitutive models are used to describe the behaviour of AAA wall, namely, linear elastic, Saint Venant Kirchhoff elastic and a phenomenological finite-strain model proposed by Raghavan et al. (*J. Biomech.* (2000) 33:475-482) called Raghavan-Vorp elastic. For a particular AAA, linear elastic and Saint Venant Kirchhoff elastic models underpredict peak wall stress and also the maximum wall displacement as compared to Raghavan-Vorp elastic model. Saint Venant Kirchhoff elastic model gives higher peak wall stress but a lower maximum wall displacement as compared to the linear elastic model. In every case, the peak wall stress is in the midway of the ends of the aneurysm sac and the central bulge location. The peak wall stress of AAA1 is about 8 % higher than that of AAA2 suggesting that AAA of higher Dhr is at a greater risk of rupture.

## ACKNOWLEDGMENTS

Not applicable.



(a)



(b)

FIG. 22: Variation of (a) maximum principal stress and (b) maximum von Mises stress in AAA2 wall over a cardiac cycle for linear, Saint Venant Kirchhoff and Raghavan-Vorp elastic models

## AUTHOR DECLARATIONS

### Conflict of Interest

The authors have no conflicts to disclose.

### Author Contributions

**G R Krishna Chand Avatar:** Conceptualization; Data curation; Formal analysis; Methodology; Software; Validation; Visualization; Writing – original draft, review & editing.

**Chinika Dangi:** Data curation; Software; Validation; Writing – review & editing. **Puneet**

**Pushkar:** Conceptualization; Formal analysis; Methodology; Software; Writing – review & editing.

## DATA AVAILABILITY STATEMENT

The data that support the findings of this study are available from the corresponding author upon reasonable request.

## REFERENCES

- <sup>1</sup>T. Canchi, S. D. Kumar, E. Y. K. Ng, and S. Narayanan, “A review of computational methods to predict the risk of rupture of abdominal aortic aneurysms,” *BioMed Research International* **2015**, 1–12 (2015).
- <sup>2</sup>S. Aggarwal, A. Qamar, V. Sharma, and A. Sharma, “Abdominal aortic aneurysm: A comprehensive review,” *Experimental and clinical cardiology* **16**, 11–15 (2011).
- <sup>3</sup>N. T. Philip, B. Patnaik, and B. Sudhir, “Hemodynamic simulation of abdominal aortic aneurysm on idealised models: Investigation of stress parameters during disease progression,” *Computer Methods and Programs in Biomedicine* **213**, 106508 (2022).
- <sup>4</sup>N. T. Philip, B. S. V. Patnaik, and S. B. J., “Fluid structure interaction study in model abdominal aortic aneurysms: Influence of shape and wall motion,” *International Journal for Numerical Methods in Biomedical Engineering* (2020), 10.1002/cnm.3426.
- <sup>5</sup>E. A. Finol, K. Keyhani, and C. H. Amon, “The effect of asymmetry in abdominal aortic aneurysms under physiologically realistic pulsatile flow conditions,” *Journal of Biomechanical Engineering* **125**, 207–217 (2003).
- <sup>6</sup>M. Unnikrishnan, A. Savlania, P. Goura, H. Verma, and R. Tripathi, “Aortic diseases in India and their management: An experience from two large centers in South India,” *Indian Journal of Vascular and Endovascular Surgery* **3**, 20–23 (2016).
- <sup>7</sup>B. W. Ullery, R. L. Hallett, and D. Fleischmann, “Epidemiology and contemporary management of abdominal aortic aneurysms,” *Abdominal Radiology* **43**, 1032–1043 (2018).
- <sup>8</sup>F. A. Lederle, “The aneurysm detection and management study screening program,” *Archives of Internal Medicine* **160**, 1425 (2000).

- <sup>9</sup>F. A. Lederle, “Prevalence and associations of abdominal aortic aneurysm detected through screening,” *Annals of Internal Medicine* **126**, 441 (1997).
- <sup>10</sup>S. S. Raut, S. Chandra, J. Shum, and E. A. Finol, “The role of geometric and biomechanical factors in abdominal aortic aneurysm rupture risk assessment,” *Annals of Biomedical Engineering* **41**, 1459–1477 (2013).
- <sup>11</sup>D. A. Vorp, M. Raghavan, and M. W. Webster, “Mechanical wall stress in abdominal aortic aneurysm: Influence of diameter and asymmetry,” *Journal of Vascular Surgery* **27**, 632–639 (1998).
- <sup>12</sup>E. A. Finol and C. H. Amon, “Blood flow in abdominal aortic aneurysms: Pulsatile flow hemodynamics,” *Journal of Biomechanical Engineering* **123**, 474–484 (2001).
- <sup>13</sup>E. Finol and C. Amon, “Flow dynamics in anatomical models of abdominal aortic aneurysms: Computational analysis of pulsatile flow,” *Acta Científica Venezolana* **54**, 43–9 (2003).
- <sup>14</sup>A. J. Boyd, D. C. Kuhn, R. J. Lozowy, and G. P. Kulbisky, “Low wall shear stress predominates at sites of abdominal aortic aneurysm rupture,” *Journal of Vascular Surgery* **63**, 1613–1619 (2016).
- <sup>15</sup>A. Venkatasubramaniam, M. Fagan, T. Mehta, K. Mylankal, B. Ray, G. Kuhan, I. Chetter, and P. McCollum, “A comparative study of aortic wall stress using finite element analysis for ruptured and non-ruptured abdominal aortic aneurysms,” *European Journal of Vascular and Endovascular Surgery* **28**, 168–176 (2004).
- <sup>16</sup>D. Bluestein, L. Niu, R. T. Schoepfoerster, and M. K. Dewanjee, “Steady flow in an aneurysm model: Correlation between fluid dynamics and blood platelet deposition,” *Journal of Biomechanical Engineering* **118**, 280–286 (1996).
- <sup>17</sup>S. Lin, X. Han, Y. Bi, S. Ju, and L. Gu, “Fluid-structure interaction in abdominal aortic aneurysm: Effect of modeling techniques,” *BioMed Research International* **2017**, 1–10 (2017).
- <sup>18</sup>M. L. Raghavan, M. W. Webster, and D. A. Vorp, “Ex vivo biomechanical behavior of abdominal aortic aneurysm: Assessment using a new mathematical model,” *Annals of Biomedical Engineering* **24**, 573–582 (1996).
- <sup>19</sup>C. M. Scotti, A. D. Shkolnik, S. C. Muluk, and E. A. Finol, “Fluid-structure interaction in abdominal aortic aneurysms: Effects of asymmetry and wall thickness,” *BioMedical Engineering OnLine* **4** (2005), 10.1186/1475-925x-4-64.

- <sup>20</sup>G. Martufi, E. S. D. Martino, C. H. Amon, S. C. Muluk, and E. A. Finol, “Three-dimensional geometrical characterization of abdominal aortic aneurysms: Image-based wall thickness distribution,” *Journal of Biomechanical Engineering* **131** (2009), 10.1115/1.3127256.
- <sup>21</sup>E. Perez, L. Rojas-Solorzano, and E. Finol, “Geometric predictors of abdominal aortic aneurysm maximum wall stress,” *Chemical Engineering Transactions* **49**, 73–78 (2016).
- <sup>22</sup>W. A. Cappeller, H. Engelmann, S. Blechschmidt, M. Wild, and L. Lauterjung, “Possible objectification of a critical maximum diameter for elective surgery in abdominal aortic aneurysms based on one- and three-dimensional ratios,” *J Cardiovasc Surg (Torino)* **38(6)**, 623–628 (1997).
- <sup>23</sup>M. Raghavan and D. A. Vorp, “Toward a biomechanical tool to evaluate rupture potential of abdominal aortic aneurysm: identification of a finite strain constitutive model and evaluation of its applicability,” *Journal of Biomechanics* **33**, 475–482 (2000).
- <sup>24</sup>I. L. de Oliveira, *Using foam-extend to assess the influence of fluid-structure interaction on the rupture of intracranial aneurysms* (Universidade Estadual Paulista, Brazil, 2017).
- <sup>25</sup>A. Sequeira, “Hemorheology: Non-Newtonian Constitutive Models for Blood Flow Simulations,” in *Lecture Notes in Mathematics* (Springer International Publishing, 2018) pp. 1–44.
- <sup>26</sup>K. M. Khanafer, P. Gadhoke, R. Berguer, and J. L. Bull, “Modeling pulsatile flow in aortic aneurysms: effect of non-Newtonian properties of blood,” *Biorheology* **43**, 661–679 (2006).
- <sup>27</sup>Y. I. Cho and K. R. Kensey, “Effects of the non-Newtonian viscosity of blood on flows in a diseased arterial vessel. Part 1: Steady flows,” *Biorheology* **28**, 241–262 (1991).
- <sup>28</sup>J. Biasseti, F. Hussain, and T. C. Gasser, “Blood flow and coherent vortices in the normal and aneurysmatic aortas: a fluid dynamical approach to intra-luminal thrombus formation,” *Journal of The Royal Society Interface* **8**, 1449–1461 (2011).
- <sup>29</sup>T. Belytschko, W. K. Liu, and B. Moran, *Nonlinear Finite Elements for Continua and Structures* (John Wiley and Sons, Ltd, 2014).
- <sup>30</sup>G. Holzapfel, *Nonlinear solid mechanics: a continuum approach for engineering* (Wiley, Chichester New York, 2000).
- <sup>31</sup>E. W. V. Chaves, *Notes on Continuum Mechanics* (Springer Netherlands, 2013).

- <sup>32</sup>H. Jasak and H. G. Weller, “Application of the finite volume method and unstructured meshes to linear elasticity,” *International Journal for Numerical Methods in Engineering* **48**, 267–287 (2000).
- <sup>33</sup>Y. C. Fung, *Biomechanics* (Springer New York, 1990).
- <sup>34</sup>C. V. Krishna, V. C. Suja, P. N. Watton, J. H. Arakeri, and N. Gundiah, “Shear stress rosettes capture the complex flow physics in diseased arteries,” *Journal of Biomechanics* **104**, 109721 (2020).
- <sup>35</sup>A. Ribes and C. Caremoli, “Salome platform component model for numerical simulation,” in *31st Annual International Computer Software and Applications Conference - Vol. 2 - (COMPSAC 2007)* (IEEE, 2007).
- <sup>36</sup>F. Juretic and M. Baburic, “cfmesh: A library for polyhedral mesh generation,” <https://cfmesh.com/cfmesh/> (2014), accessed on 2021-06-11.
- <sup>37</sup>J. Jeong and F. Hussain, “On the identification of a vortex,” *Journal of Fluid Mechanics* **285**, 69 (1995).
- <sup>38</sup>X. Zhang, T. Watanabe, and K. Nagata, “Reynolds number dependence of the turbulent/non-turbulent interface in temporally developing turbulent boundary layers,” *Journal of Fluid Mechanics* **964** (2023), 10.1017/jfm.2023.329.
- <sup>39</sup>Iago Lessa de Oliveira, *Private Communication* (None, 2021).
- <sup>40</sup>L. D. Browne, K. Bashar, P. Griffin, E. G. Kavanagh, S. R. Walsh, and M. T. Walsh, “The role of shear stress in arteriovenous fistula maturation and failure: A systematic review,” *PLOS ONE* **10**, e0145795 (2015).
- <sup>41</sup>I. L. Oliveira, G. B. Santos, J. Miltzer, C. E. Baccin, R. T. Tatit, and J. L. Gasche, “A longitudinal study of a lateral intracranial aneurysm: identifying the hemodynamic parameters behind its inception and growth using computational fluid dynamics,” *Journal of the Brazilian Society of Mechanical Sciences and Engineering* **43** (2021), 10.1007/s40430-021-02836-6.
- <sup>42</sup>O. Mutlu, H. E. Salman, H. Al-Thani, A. El-Menyar, U. A. Qidwai, and H. C. Yalcin, “How does hemodynamics affect rupture tissue mechanics in abdominal aortic aneurysm: Focus on wall shear stress derived parameters, time-averaged wall shear stress, oscillatory shear index, endothelial cell activation potential, and relative residence time,” *Computers in Biology and Medicine* **154**, 106609 (2023).